RESEARCH ARTICLE
SPACE PHYSICS: MAGNETOSPHERIC PHYSICS

Earth and Planetary Physics
9: 375–386, 2025
doi: 10.26464/epp2024069

The intensity of geomagnetic storms associated with the interplanetary magnetic field and solar wind parameters during Solar Cycle 24

Anwar Santoso[1,2], Sismanto Sismanto[3*], Rhorom Priyatikanto[1], Eddy Hartantyo[3], and Dyah R. Martiningrum[4,5]

[1]Research Center for Space, National Research and Innovation Agency, Bandung 40173, Indonesia;

[2]Physics Department, Faculty of Mathematics and Natural Sciences, Gadjah Mada University, Yogyakarta, Indonesia;

[3]Geophysics Laboratory, Physics Department, Faculty of Mathematics and Natural Sciences, Gadjah Mada University, Yogyakarta, Indonesia;

[4]Research Center for Climate and Atmosphere, National Research and Innovation Agency, Bandung 40173, Indonesia;

[5]School of Graduate Studies, Faculty of Science, Universiti Teknologi Malaysia, Johor Bahru, Malaysia

Key Points:

- Statistical model is practical for forecasting geomagnetic storm events based on the characteristics of the incoming solar wind and the linterplanetary magnetic field.
- Using a regression formula, the model has a coefficient of determination of 0.58, a root mean square error of 21.30 nT, and a mean absolute error of 15.87 nT.
- While more complex machine learning models may outperform this model, it provides a theoretically sound alternative for understanding and forecasting geomagnetic storms.

Citation: Santoso, A., Sismanto, S., Priyatikanto, R., Hartantyo, E., and Martiningrum, D. R. (2025). The intensity of geomagnetic storms associated with the interplanetary magnetic field and solar wind parameters during Solar Cycle 24. *Earth Planet. Phys.*, *9*(2), 375–386. http://doi.org/10.26464/epp2024069

Abstract: Proper knowledge of the nature of geomagnetic storms and their relationships with the conditions of the space environment at the outer part of the Earth's magnetosphere (bow shock nose) is essential to increase our resilience to space weather disturbances. In this article, we present an analysis of the interplanetary magnetic field (IMF) and solar wind parameters relevant to 100 geomagnetic storms in Solar Cycle 24. We revisit the relationship between the minimum disturbance storm time index ($Dst_{\min}$), the minimum southward IMF ($B_{S,\min}$), the maximum solar wind density ($N_{SW,\max}$) and speed ($V_{\max}$), and the lag time between the extrema (d$T(B_z, N)$, d$T(B_z, V)$). We end with a regression formula that fits the data, with a coefficient of determination of 0.58, a root mean square error of 21.30 nT, and a mean absolute error of 15.87 nT. Even though more complex machine learning models can outperform this model, it serves as a theoretically sensible alternative for understanding and forecasting geomagnetic storms.

Keywords: geomagnetic storm; interplanetary magnetic field (IMF); solar wind; space weather

1. Introduction

The Sun is the main driver of space weather because the dynamic nature of its atmosphere influences the distribution and characteristics of plasma around the Earth. In turn, the configuration of Earth's magnetosphere may be altered such that a geomagnetic storm takes place. Among several phenomena in the Sun's atmosphere, coronal mass ejections (CMEs) become the main causes of geomagnetic storms, together with the corotating interaction regions (CIRs) in interplanetary space, where the slow solar wind is compressed by the fast wind (Webb and Howard, 2012; Temmer, 2021). Geomagnetic storms with various levels of intensity can be induced by such phenomena. The impacts of the storms range from the disturbance of high-frequency radio communication (Blagoveshchensky and Sergeeva, 2019; Frissell et al., 2019) to disruption of the electrical power grid, especially in high-latitude regions (McNish, 1940; Bolduc, 2002; Pulkkinen et al., 2005; Kataoka and Ngwira, 2016; Abraha et al., 2020). Consequently, mitigation of the impacts should include the reliable forecasting of the geomagnetic storms according to the observed conditions of the Sun and the sensed configuration of the interplanetary magnetic field (IMF) around the Earth.

A high-speed streamer originating from a coronal hole or a specifically directed CME carries energetic particles and magnetic fields that propagate toward the Earth. Before reaching the Earth, an interplanetary shock (IPS) can be formed by the interaction

First author: A. Santoso, anwa011@brin.go.id
war92_2000@yahoo.com
Correspondence to: S. Sismanto, sismanto@ugm.ac.id
Received 26 MAY 2024; Accepted 25 SEP 2024.
First Published online 08 JAN 2025.

between the fast flow and the ambient solar wind, enhancing the density, temperature, and magnetic field of the wind. Upon arrival in the vicinity of the Earth, the IPS may generate a geomagnetic storm (Kataoka et al., 2005; Kilpua et al., 2017; Pitňa et al., 2021). The occurrence and intensity of geomagnetic storms are determined by the characteristics of the incoming solar wind and CME, as well as the southward IMF (negative B_z or B_S), during the reconnection stage. Both magnetopause reconnection in the dayside magnetosphere and magnetotail reconnection in the nightside magnetosphere may occur. At this stage, energetic particles are injected by the solar wind or the CME into the Earth's magnetosphere. In most cases, CME-driven storms are preceded by a CME. Coronal mass ejection-driven storms are characterized by sudden increases in southward B_S, solar wind speed (V_{SW}), and proton density (N_{SW}), often accompanied by a shock (Neugebauer and Goldstein, 1997). In contrast, CIR-driven storms are marked by fluctuating increases in V_{SW}, decreases in the N_{SW}, and fluctuations in the IMF (B_S; Shen XC et al., 2017; Pandya et al., 2019). Denton et al. (2006) reviewed the distinctions between storm-driven CMEs and storm-driven CIRs, which are primarily influenced by the solar wind, and examined the differences in their signatures.

The amount of energized particles in the magnetic field determines the intensity of the geomagnetic storm generated (Burton et al., 1975; Kan and Lee, 1979; Akasofu, 1981; Gonzalez, 1990). Thus, the solar wind or CME parameters and the southward-directed magnetic field (B_S), as well as ionospheric particles, play important roles in the generation of a geomagnetic storm (Burton et al., 1975; Crooker et al., 1977; Kan JR and Lee, 1979; Akasofu, 1981; Gonzalez, 1990; Zhou XY et al., 2020; Chappell et al., 2021; Ren J et al., 2023). Notably, the solar wind (with varying shapes, such as CIRs, magnetic clouds, and ejecta) becomes the most prominent driver of a geomagnetic disturbance during the solar minimum (Richardson et al., 2001; Richardson and Cane, 2012), whereas the CME takes this role during the solar maximum (Borovsky and Denton, 2006; Echer et al., 2008; Wu CC et al., 2016). Some differences have also been observed between geomagnetic storms induced by these two drivers (Borovsky and Denton, 2006). Coronal mass ejection-driven storms are more likely to threaten the electric power grid, whereas CIR-driven ones can affect space-borne assets (Pandey and Dubey, 2017).

Studies have been conducted to understand the relationships between the solar wind (or a CME) and the intensity of geomagnetic storms (Wu CC et al., 2006; Bakare and Chukwuma, 2010; Rathore et al., 2014). The ultimate aim is to provide an accurate prediction of geomagnetic storms as early as possible. Among other researchers, Verbanac et al. (2011) investigated the relationships between coronal holes as the source of high-speed solar wind and the geomagnetic storm indices (daily global geomagnetic activity, *Ap*; electrojet auroral activity in high latitudes, *AE*; and geomagnetic activity in middle-low-equator latitudes, *Dst*). They found that the combination of the solar wind speed (*V*) and the IMF (*B*) served as crucial indicators of energy transfer from the solar wind to the magnetosphere. Nagatsuma et al. (2015) tested the relationship between the *Dst* index and solar wind parameters by using the extreme storm of March 13–14, 1989, as a case study. At the extreme end of geomagnetic storms, the solar wind dawn–dusk electric field (vB_z) is believed to be an important factor in characterizing the impact on the magnetosphere (Burton et al., 1975; Kan JR and Lee, 1979; Akasofu, 1981; Larrodera, 2021).

Several methods are used to understand the relationship between the solar wind, IMF characteristics, and the induced geomagnetic storm. Many statistical models have been used to establish predictive models (Kugblenu et al., 1999; Stepanova et al., 2008; Kim et al., 2014; Podladchikova et al., 2018; Chakraborty and Morley, 2020). On one end, a simple regression model with several variables becomes an alternative with more easily discernable implications (Khabarova, 2008). On the other end, machine learning techniques have been used to forecast incoming geomagnetic storms. The neural network (NN) has become a tool of choice in some studies (Kugblenu et al., 1999; Lethy et al., 2018; Chakraborty and Morley, 2020; Park et al., 2021), whereas more recent studies have combined NNs with other models, such as support vector machines and long short-term memory networks, into an ensemble model (Xu SB et al., 2020). Depending on the data used, the reported correlation coefficients (*R*) of those statistical models have ranged from 75% to 95%.

Despite its simplicity, the regression model still possesses an interesting feature worth exploring. For instance, Khabarova (2008) presented a relationship between the minimum B_S, the maximum density of the solar wind (*N*) before the storm, the lag time (d*t*) of the storm, and the minimum value of the *Dst* index. The minimum *Dst* was assumed to be a function of the dynamic pressure of the solar wind (*P*), which was related to the first three parameters mentioned (*N*, *V*, B_S). Khabarova (2008) reported an *R* of 0.91 for the case of 30 geomagnetic storms from 1995 to 2001 ($-140 \leq Dst \leq -40$ nT). Even though the solar wind speed (*V*) is thought to be a crucial factor, this parameter was not taken into account in the model presented by Khabarova (2008).

The reconnection between the IMF and the magnetosphere, either at the dayside magnetopause or at the nightside magnetotail, triggers the transport of energized ions to the inner parts of the magnetosphere. This movement causes a disturbance of the ring current system in the magnetosphere. At the low-latitude region, this disturbance can be represented by a decrease in the *Dst* index. The energy injected into the ring current is proportional to the solar wind speed (Burton et al., 1975) and density (Khabarova, 2008). When the solar wind with a southward magnetic field ($B_z < 0$) collides with the magnetosphere, an injection of energy will occur and a geomagnetic storm will emerge. Burton et al. (1975) stated that speed is the most dominant solar wind parameter contributing to the formation of a geomagnetic storm, especially when the B_z is negative. The B_z determines the efficiency of energy injection into ring currents, which is represented by a significant depression of the geomagnetic disturbance index (i.e., the *Dst* index). In contrast, when the B_z is positive, the energy injection is less efficient. We can say that the intensity of a geomagnetic storm does not directly depend on the solar wind speed (*V*) because the relationship is not linear (Rangarajan and Barreto, 2000; Wu CC and Lepping, 2002).

The solar wind speed is not the only parameter affecting the intensity of geomagnetic storms. The dynamic pressure exerted by the solar wind depends on its speed and density. Therefore, we consider including both parameters in the model. We understand

that the importance of V and N may vary by case. Previously, Santoso (2010) analyzed 44 geomagnetic storms from 1996 to 2001 and found that in 20% of the cases, the intensity of the storms was predominantly affected by V, whereas 41% were strongly related to N. In the remaining cases (39%), both parameters appeared to be equally influencing. However, a quantitative exploration of this aspect needs to be performed.

In this work, we aim to develop a statistical model to estimate geomagnetic storm events based on the characteristics of the incoming solar wind and the southward IMF. We focus on the moderate and strong events in Solar Cycle 24. Departing from the view of Khabarova (2008, and references therein), we apply some simple models to the data.

Geomagnetic storms can cause disturbances in the geomagnetic field and ionosphere. Geomagnetic field disturbances can induce geomagnetically induced currents. These geomagnetically induced currents are quasi-direct currents with very low frequencies that can cause half-cycle saturation in power grids, leading to overheating and potentially triggering transformer fires. The most famous half-cycle saturation event in a power transformer occurred in the Hydro-Québec transformer in Canada, triggered by a geomagnetic storm on March 13, 1989, which caused a blackout in two-thirds of Canada's territory for 9 h and resulted in billions of dollars in damage.

2. Data

We compile data associated with 100 geomagnetic storm events ($Dst < -50$ nT) that occurred from 2008 to 2020 (see Table S1 in Supplementary Materials). We use the hourly Dst index from the World Data Center for Geomagnetism, Kyoto University (https://wdc.kugi.kyoto-u.ac.jp/wdc/Sec3.html). The Data Center provided the final Dst. To characterize the conditions of the space environment before the storm events, we acquire several parameters from the National Aeronautics and Space Administration's (NASA's) OMNIWeb service (https://omniweb.gsfc.nasa.gov/cgi/nx1.cgi). Among the parameters relevant to the study of the heliosphere, we download the northward–southward IMF, the solar wind density, and the solar wind speed. These parameters were derived from measurements by the Wind and Advanced Composition Explorer (ACE) satellites situated at the Sun–Earth Lagrange L1 point (1.5 million km from Earth). Time shifting is applied to the data such that the parameters represent the solar wind conditions at the Earth's bow shock nose. Continuous measurement at this location provides important data for short-term space weather prediction.

Additionally, we identify the main driver of the geomagnetic storms, either CMEs or solar wind-induced CIRs. For this purpose, we depart from the work of Pandya et al. (2019), Chi YT et al. (2016, 2018), and Hajra and Sunny (2022), in which the drivers of the storms were determined according to the solar wind data at L1. We extend the list from Pandya et al. (2019) with storms in 2008–2012 and 2018–2020 so that the data cover the entire Solar Cycle 24. In this study, the storm-driven CMEs and storm-driven CIRs are identified by using IMF B_z data and solar wind parameters (N, V, and P) at the L1 point, with insights drawn from the findings of Neugebauer and Goldstein (1997), Denton et al. (2006), and Pandya et al. (2019).

For the identification of CMEs, we refer to the CME catalog provided by NASA's Coordinated Data Analysis Workshop (https://cdaw.gsfc.nasa.gov/CME_list/). This catalog is based on real-time observations by the Large-Angle Spectroscopic Coronograph instrument at the Solar and Heliospheric Observatory (SOHO/LASCO). We define an Earth-directed ejection as a CME with a positional angle of 270° and an angular width of more than 30°. Before a geomagnetic storm event, some increases in solar wind density and speed at the Earth's bow shock nose are observed. In parallel with these changes, a depression of the southward IMF is observed. During an IPS, the interaction between the solar wind and the magnetosphere determines the presence or absence of energy injection into the ring current. If the IMF B_z direction during the IPS tends to be southward (sustained for a long duration and with a strong southward intensity), substantial energy will be injected into the magnetospheric ring current. All solar wind parameters are involved in dynamic pressure collisions, and each plays a role in determining the amount of energy injected into the ring current, although the exact proportions and dominance of these roles are still uncertain. Initially, it was known that the energy injected into the ring current is proportional to $E = VB_z$, indicating that geomagnetic storm events are predominantly influenced by V. Recently, however, parameter N has also been considered in studies on geomagnetic storms stemming from the mechanism of dynamic pressure. Several research studies have discussed the role of N in geomagnetic storm formation, in addition to the dominant role of V (Lyatsky and Tan A, 2003; Khabarova, 2008; Xu D et al., 2009; Weigel, 2010; Saikin et al., 2016).

On the basis of the hourly data mentioned, we visually identify the magnitude and the time of Dst_{min} and the preceding time of the minimum southward IMF (B_z), the maximum solar wind density (N_{max}), and the maximum speed (V_{max}). Thus, we can compute the time difference between Dst_{min} and B_z ($dT(B_z, Dst)$), between B_z and N ($dT(B_z, N)$), and between B_z and V ($dT(B_z, V)$). Occasionally, we cannot identify any peak of V or N before the moment of Dst_{min} such that we assume the time difference to be zero. Table S1 (in the Supplementary Materials) summarizes the parameters associated with 100 of the geomagnetic storm events analyzed in this study. Figure 1 shows examples of the shapes of CME-driven and CIR-driven storm events, with criteria referring to Shen XC et al. (2017).

To validate our identification of the storm driver, we refer to the works of Chi YT et al. (2016, 2018), mainly for storms that occurred before 2016, Pandya et al. (2019) for events from 2012 to 2017, and Hajra and Sunny (2022) for CIR-driven storms from 2008 to 2019. Among the 100 geomagnetic storms listed in the table, we match 65 with at least one of the reference catalogs and have 11 mismatches; we can find no comparison for the remaining 24 events. Thus, the overall accuracy of our identification is approximately 85%. In most of the mismatches, we can identify the events as CME driven because of the occurrence of CMEs before the storms, whereas Hajra and Sunny (2022) defined them as CIR-driven storms.

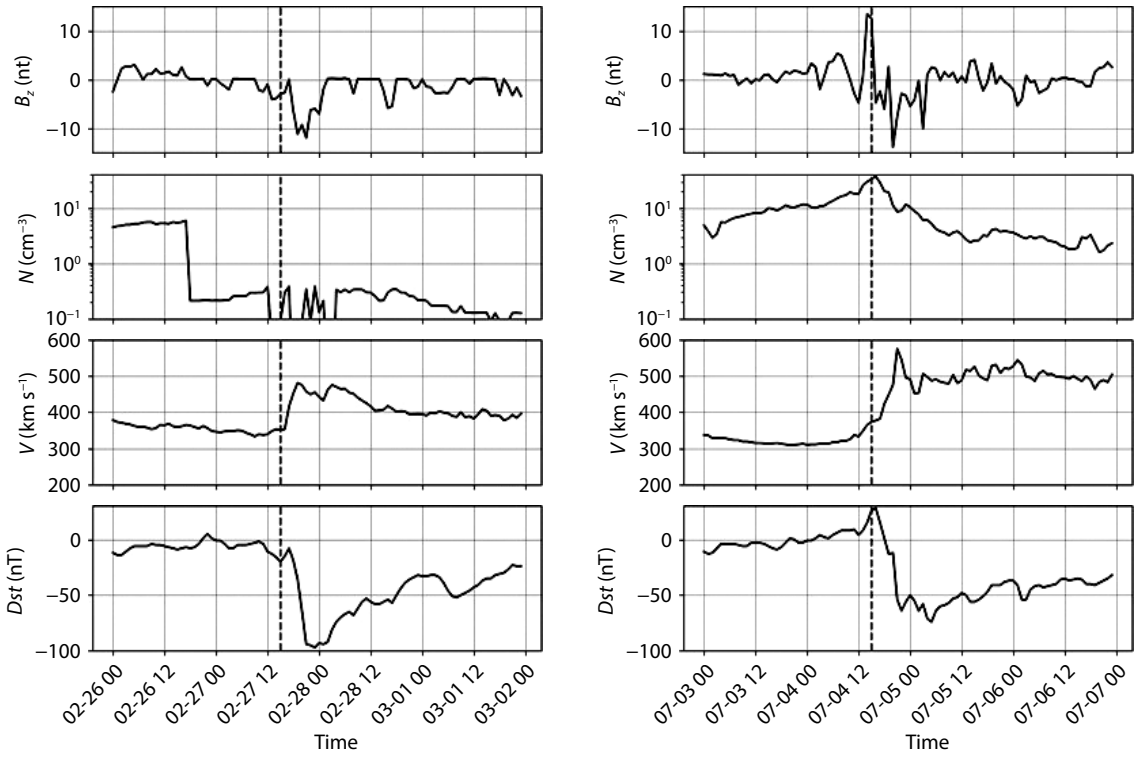

Figure 1. (Left) Profiles of a CME-driven storm on February 27, 2014 (a), and (Right) profiles of a CIR-driven storm on July 4, 2015 (https://omniweb.gsfc.nasa.gov/form/dx1.html). The shock arrival in the left profile and the stream interface in the right profile is marked with vertical dashed lines. In the left profile, all solar wind parameters increased simultaneously at 15:00 UT on February 27, 2014. In the right profile, only the solar wind speed begins to increase at 15:00 UT, while the solar wind density and pressure start to decrease (Shen XC et al., 2017). The time is in UT, the format is mm-dd hh, where mm represents the month, dd represents the day, and hh represents the hour.

3. Method

Khabarova (2008) demonstrated that the maximum solar wind density (N) and the southward-directed magnetic field (B_S) are important variables for predicting the intensity of a geomagnetic storm, as indicated by the $Dst_{\min}$. According to data acquired from 1995 to 2001 (around the solar minima), Khabarova (2008) found the following relationship:

$$Dst_{\min} = 4.5P + 6.5, \tag{1}$$

with

$$P = B_z - \sqrt{N\mathrm{d}T_N}. \tag{2}$$

Here, $\mathrm{d}T_N$ represents the time lag or time difference between the onset of the maximum N and the moment of the $Dst_{\min}$ (the unit in hours). This relationship can be expanded to include the speed (V) in the calculation. We assume that the $Dst_{\min}$ follows the equation below:

$$Dst_{\min} = \alpha B_z^a + \beta N^b + \gamma V^c + \delta \mathrm{d}T_{(B_z,N)}^d + \in \mathrm{d}T_{(B_z,V)}^e + \zeta, \tag{3}$$

where V and N are the maximum speed ($V_{\max}$) and density ($N_{\max}$) of the solar wind before the B_z reaches its minimum. The time difference between the onset of $N_{\max}$ and the minimum B_z is indicated by $\mathrm{d}T(B_z, N)$, whereas the time difference between the onset of $V_{\max}$ and the minimum B_z is denoted by $\mathrm{d}T(B_z, V)$.

We experiment with several possible values of power a, b, c, d, and e that range from 0.5 to 2.0 and fit the entire dataset by using linear regression to obtain the coefficients α, β, γ, δ, $\in$, and ζ. In detail, we try all 1875 possible combinations of the exponents and fit the data using those combinations. For each combination (e.g., $a = b = c = d = e = 1$), we obtain the coefficients and compute the coefficient of determination (R^2), root mean square error (RMSE), and mean absolute error (MAE) as the measure of fit. The best combination is assessed based on the R^2.

4. Results and Discussion

4.1 Characteristics

In general, the characteristics of the storms in our dataset can be seen from some statistical figures. The intensity of the storms is indicated by the median $Dst_{\min}$ of −85 nT, with an interquartile range (IQR) of 38 nT. Before the storms, the values of the B_z have a median of −12 nT and an IQR of 6 nT. The median value of the N is 95 particles/cm^3, whereas the IQR is 19. In terms of solar wind speed, the storms are associated with a maximum speed of V, with a median of 491 km/s and an IQR of 160 km/s. The lag times between the minimum B_z and Dst have a first quartile (Q_1), second quartile (Q_2), and third quartile (Q_3) of 2, 3, and 5 h, respectively. The typical time difference between B_z and N is slightly lower, as indicated by a Q_1 of 1 h, a Q_2 of 3 h, and a Q_3 of 5 h. Last, $\mathrm{d}T(B_z, V)$ tends to be shorter (Q_1 of 0 h, Q_2 of 1 h, and Q_3 of 3 h). In 41% of cases, we cannot identify a significant peak of V before the moment of $Dst_{\min}$ such that we set $\mathrm{d}T(B_z, V) = 0$. These statistical properties of the data, mainly the ones related to the timing of the storms, dictate that the IMF and solar wind characteristics at L1 (or the Earth's bow shock nose) are essential for short-term geomag-

Table 1. Statistical summary of the storm parameters analyzed in this study.

	Dst_{min} (nT)	B_z (nT)	N_{sw} (cm^{-3})	V_{sw} (km/s)	$dT_{B_z,N_{sw}}$ (h)	$dT_{B_z,V_{sw}}$ (h)	$dT_{B_z,Dst}$ (h)
CIR and CME-driven storm							
Average	−85	−12	19	491	3	2	4
StDev	33	5	13	103	3	3	3
Q_1	−101	−14	9	407	1	0	2
Q_2	−74	−11	15	482	3	1	3
Q_3	−60	−8	28	569	5	3	5
CIR-driven storm							
Average	−71	−10	19	489	3	2	4
StDev	23	3	12	94	2	2	3
Q_1	−75	−12	10	419	1	0	2
Q_2	−66	−9	15	486	3	0	3
Q_3	−56	−7	27	551	5	2	6
CME-driven storm							
Average	−97	−13	20	489	4	3	4
StDev	36	5	14	109	3	3	3
Q_1	−116	−17	9	397	1	0	2
Q_2	−88	−12	14	481	3	2	3
Q_3	−72	−8,9	29,5	570	5	4	5

netic storm prediction. A statistical summary of the storm parameters analyzed in this study is shown in Table 1.

Figure 2 visualizes the distribution of CME-driven and CIR-driven storms over the time span of Solar Cycle 24. The intensity of each storm is also presented. We can see that the CIR-driven storms are more common during the solar minima, whereas the majority of severe storms (Dst < −200 nT) are associated with CMEs. Statistically, CME-driven storms are preceded by a lower B_z depression and a higher N compared with CIR-driven storms (Gonzalez et al., 1999; Borovsky and Denton, 2006). However, our dataset does not show any significant difference between the V associated with CME- and CIR-driven storms.

4.2 The Best Model

Figure 3 summarizes the results of our experimentation on the use of a different set of [a, b, c, d, e] in Equation (3). We aim to find simple relationships that can then be interpreted physically. There are 1875 possible combinations of those parameters, as we consider $a \in$ [0, 1, 2], whereas the remaining parameters are [0, 1/2, 1, 3/2, 2]. For each pair of parameters (e.g., a and b) with certain values, we compute the median R^2 and display it in Figure 3. A higher R^2 indicates a better combination. The mapped values of R^2 can be used as a guide to choose the parameters, as an alternative to a single selection based on the maximum score among all possible combinations. Our justifications for the model that provides the best predictions are as follows.

Among three possible values, a = 1 provides a better model, as indicated by the higher R^2. The scores vary slightly as b changes, but either b = 1/2 or b = 1 will be a good choice as the power of N. As Khabarova (2008) explained, many studies have shown that the more intense the pressure exerted on the magnetosphere, the more intense will be the storm generated. As Burton et al. (1975) pointed out, the depression of the Dst is proportional to the square root of the dynamic pressure. Reasonable choices for the last two parameters are d = e = 1/2. From the bottom panels of Figure 2, we can see that the model with e = 1/2 produces a higher R^2, whereas the variation of d only marginally alters the R^2.

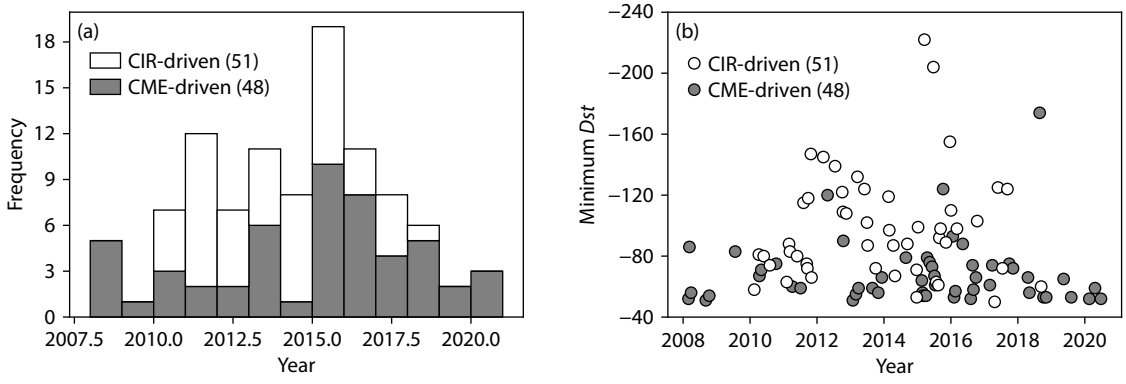

Figure 2. The distribution of the geomagnetic storms analyzed in this study, both in time–space (a) and time–intensity space (b).

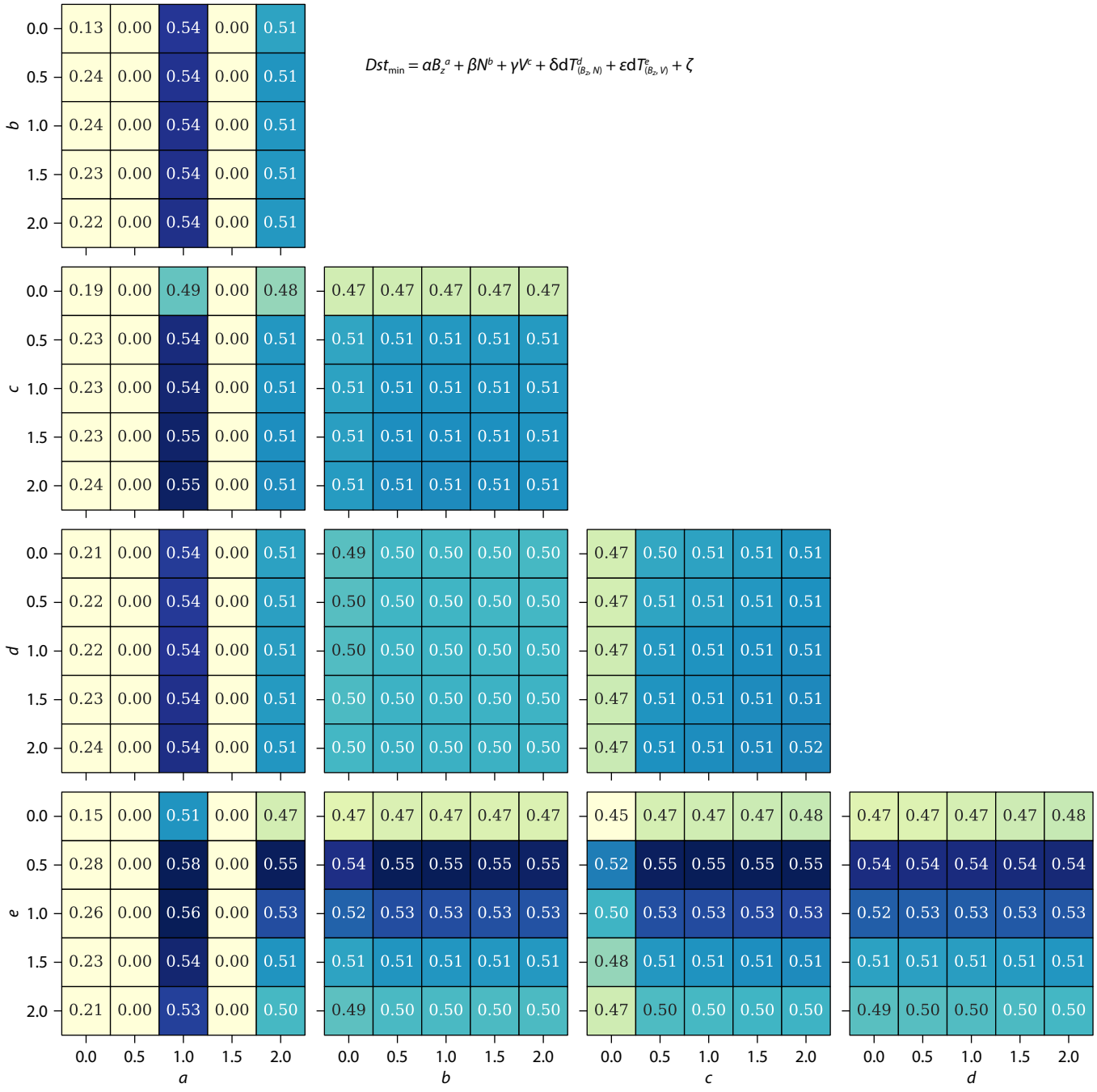

Figure 3. The color-coded median R^2 from the model (Equation (3)) with particular choice of parameter *a*, *b*, *c*, *d*, *e*.

Although a higher value of *d* yields a higher score, we prefer to use 1/2 such that both terms, d*T*(*B*, *N*) and d*T*(*B*, *V*), have the same dimensions. In the end, we obtain the following equation that fits the data:

$$Dst_{min} = aB_z + \beta\sqrt{N} + \gamma V + \delta\sqrt{dT_{(B_z,N)}} + \epsilon\sqrt{dT_{(B_z,V)}} + \zeta, \quad (4)$$

with the regression coefficients of $\alpha = 4.46$, $\beta = 2.30$, $\gamma = 0.08$, $\delta = 0.48$, $\epsilon = 8.99$, and $\zeta = 25.89$. The R^2 for this model is 0.58, whereas the RMSE is 21.30 nT and the MAE is 15.86 nT. To examine how the scores are affected by the data used for the evaluation, we randomly select 25 storms and use this subset to recalculate the score. This process is repeated 10 times to obtain statistically sound results. Eventually, using Equation (4) and the accompanying coefficients, we obtain an R^2 of 0.53 ± 0.13, an RMSE of 20.72 ± 4.53 nT, and an MAE of 15.74 ± 2.82 nT. Additionally, we categorize the data based on the major driver, either CME or CIR. The evaluation of Equation (4) when using data from CME-driven storms yields an R^2 of 0.49, an RMSE of 25.33 nT, and an MAE of 19.48 nT. Even lower goodness of fit comes from the evaluation using data associated with CIR-driven storms, that is, an R^2 of 0.41, an RMSE of 16.51 nT, and an MAE of 12.29 nT.

These scores depend on the characteristics of the data. For example, more severe storms are CME driven such that we have a broader range of Dst_{min} that yields a higher R^2. In contrast, CIR-driven storms tend to be moderate and concentrated at a median value of $Dst_{min} \approx -60$ nT. Consequently, although the errors are

reduced, the R^2 for this dataset is also lower. As mentioned in Section 3, the overall accuracy of our categorization is 85%, compared with extensive catalogs found in the literature. We argue that the difference in driver identification does not affect our results, especially the relationship represented by Equation (4).

4.3 Deviating Cases

Figure 4 presents a comparison between the predicted and observed depression of *Dst* for 100 geomagnetic storms in Solar Cycle 24. This cycle is known as a less active one in some regards. Besides having a smaller amplitude in terms of the number of sunspots, it has a lower average solar wind speed (Watari, 2018). The median and average of the absolute error are 15.8 nT and 11.5 nT, respectively. Six geomagnetic storm events are cases in which the absolute error exceeds 40 nT. Among those deviating cases, two are identified as CIR-driven storms (2016-08-03, 2018-08-26), whereas the others are associated with CME-driven storms (2011-10-25, 2015-03-17, 2015-06-23, 2017-07-16). In terms of intensity, two are categorized as moderate storms (-100 nT $\leq Dst_{\rm min} < -50$ nT), two are strong storms (-200 nT $\leq Dst_{\rm min} < -100$ nT), and the remaining two are super-strong storms ($Dst_{\rm min} < -200$ nT).

The identification of the local extrema becomes an intricate part of the data extraction that affects the accuracy of the model. In these deviant cases, the hourly IMF and solar wind parameters show complex properties before the dip of the *Dst*. Multiple episodes of IMF enhancement increase the difficulty of characterizing the space environment before the storms. The two super-strong CME-driven storms have this characteristic (Reiff et al., 2016; Wu CC et al., 2016). In those cases, abrupt increases in the solar wind speed are measured approximately one day before the onset of the minimum *Dst*. Those increases are followed by shallower declines such that the identification of the maximum plasma speeds can be inconsistent with the other cases.

4.4 Comparison with Other Studies

Some studies have aimed to establish models of *Dst* depression based on the observed IMF and solar wind parameters. Benchmarking our results with their results is of interest. Kugblenu et al. (1999) used an NN to predict the *Dst*, with the solar wind, IMF, and *Dst* as inputs. The training data consisted of moderate storms (*Dst* < −50 nT) from 1972 to 1982 (Solar Cycles 20–21). They obtained extremely good agreement between the prediction and the observation, especially during the recovery phase. The correlation coefficient was more than 0.95, whereas the average relative variance was 10% or less, meaning that more than 90% of the observed *Dst* variance was predictable by that machine learning model. Stepanova et al. (2008) used feed-forward networks with one hidden layer to forecast the *Dst* variation. The solar wind parameters, polar cap index, and *AE* index acquired from 1999 to 2000 (Solar Cycle 23) were used as inputs. The majority of cross-correlation coefficients between the predicted and observed *Dst* of strong geomagnetic storms were situated between 0.80 and 0.90.

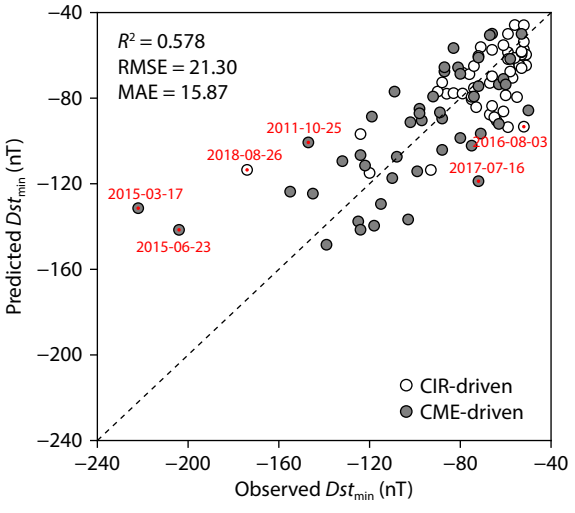

Figure 4. The correlation between observed and predicted $Dst_{\rm min}$.

Gruet et al. (2018) used a combination of the long short-term memory NN and a Gaussian process model with data from 2001 to 2014 (Solar Cycles 23–24). This model yielded great accuracy in forecasting the *Dst* index from 1 to 6 h ahead, with an correlation coefficient *r* always higher than 0.87 and an RMSE lower than 9.86 nT. Lethy et al. (2018) used an artificial NN that was trained on data from 2007 to 2015 (Solar Cycle 24). Several artificial NN structures were tested, and the best results obtained were an *r* of 0.87 for prediction 2 h in advance and an *r* of 0.86 for prediction 12 h in advance. For Solar Cycle 24, Podladchikova et al. (2018) reviewed the performance of the Storm Focus forecasting service and summarized that in real-time operation, 87% of storms were correctly predicted, whereas the reanalysis running on final OMNI data successfully predicted 97% of storms. Recently, Nuraeni et al. (2022) experimented with a nonlinear autoregressive exogenous algorithm to predict variations in the *Dst* index. That model was trained on data from 1997 to 2000 (Solar Cycle 23). Testing the model with data acquired in 2021 yielded an RMSE of 5–20 nT during quiet days and 18–45 nT during disturbed days.

Conversely, simpler models that involve linear statistics (e.g., regression) tend to have a lower score. For instance, Kim et al. (2010) established a model of the *Dst* index during CME-driven storms from 1997 to 2003 (Solar Cycle 23) and obtained an *r* of 0.44 for their prediction. Al-Feadh and Al-Ramdhan (2019) noted that the *r* score between the number of sunspots and the *Dst* index was −0.28, whereas the *r* score between the CME sky plane speed and the *Dst* index was −0.244. Kim et al. (2014) used CMEs and solar wind parameters from 1997 to 2003 and a simple model. They concluded that among the 55 moderate and stronger storms in Solar Cycle 23, 15 events were incorrectly forecasted when using CME parameters, whereas 12 other cases could be properly predicted based on solar wind conditions. In brief, most machine learning-based *Dst* prediction models were able to achieve relatively high *r* scores (0.80 or more), whereas the simpler models that relied on linear statistics achieved significantly lower *r* scores. In our study, the *r* score achieved for the fitting was ~0.70, which is relatively good. However, the score is likely to be lower when the testing dataset is somewhat different from the dataset we used for the fitting.

4.5 Physical Interpretation

Both CMEs and CIRs can lead to geomagnetic storms (Umar et al., 2023; Anoke-Uzosike et al., 2024). In the solar wind–magnetosphere coupling, as the merging rate on the dayside changes and

the reconnection rate in the geomagnetic tail fluctuates, the solar wind dynamic pressure determines the overall size and shape of the magnetosphere. Statistical studies generally suggest that the best predictor of geomagnetic storms (the *Dst* index) is not predominantly dependent on *N* (Burton et al., 1975; Ballatore and Gonzalez, 2003). They consider that the energy of the ring current is proportional to the upstream parameter: VB_S , where *V* is the solar wind speed and B_S is the southward direction component of the IMF. However, recent studies have shown that *N* plays an important role as a mediator in the transfer of energy from the solar wind to the magnetosphere that triggers geomagnetic storms through solar wind dynamic pressure, $P_{dyn} = 16726\ e^{-6}\ NV^2$ (nPa), where N_{sw} is the solar wind proton density (cm^{-3}) and *V* is the solar wind speed (km s^{-1}; Lopez et al., 2004; Borovsky and Denton, 2006; Khabarova, 2008; Xie XH et al., 2008; Weigel, 2010; Rathore et al., 2014; Umar et al., 2023). Weigel (2010) concluded that *N* modifies the geoefficiency, or the ability of the solar wind electric field, VB_S, to create geomagnetic storms. The impulse response method also predicts that *N* can explain differences in geoefficiency, such as the inverse of the solar wind dynamic pressure. Although the geoefficiency effect is substantial, its influence is small in relation to large geomagnetic storms because large geomagnetic storms also have high density. Rathore et al. (2014) showed that *N* and temperature are not notably effective in producing geomagnetic storms. Instead, *N* and *V* have a competitive effect in producing geomagnetic storms, especially on a large scale. Cheng LB et al. (2020) analyzed the superstorm that occurred on March 31, 2001, and found that the solar wind density played a substantial role in transferring solar wind energy into the magnetosphere, along with the southward magnetic field, and that the solar wind speed supported the conclusion obtained by Kataoka et al. (2005) and Weigel (2010).

Equation (3) in this work is used based on the understandings derived from the results of prior researchers (i.e., Lopez et al., 2004; Borovsky and Denton, 2006; Khabarova, 2008; Xie D et al., 2008; Weigel, 2010; Rathore et al., 2014; Umar et al., 2023) through polynomial equations. This polynomial equation describes the competitive effect of *N* and *V* parameters in generating each geomagnetic storm (Rathore et al., 2014). Regarding the time lag (d*T*), Khabarova (2008) and Weigel (2010) showed its role in the interaction between the solar wind and the magnetosphere in generating geomagnetic storms as follows: When the impulse response model is used, which incorporates the time lag in the response of the *Dst* index to solar wind variations, the solar wind electric field gives the best results or the same results as the suggested complex coupling function. Weigel (2010) indicated that (1) the proper place for *N* to appear in the model may be in the transfer function rather than in the coupling function; and (2) if correlation studies do not include a time lag, then the complex coupling function will be a better predictor than the solar wind electric field alone, but its advantage diminishes when the time lag is included in the model.

5. Conclusions

In this study, we perform a statistical analysis of the IMF and solar wind parameters associated with 100 geomagnetic storms (*Dst* of <−50 nT) in Solar Cycle 24. We experiment with a model that relates the minimum *Dst* to certain parameters, namely the minimum southward IMF (B_z), the maximum solar wind density (*N*) and speed (*V*), and the lag between the extrema (d$t(B_z, N)$, d$T(B_z, V)$). On the basis of the analysis, we find that the Dst_{min} is estimated by a linear combination of B_{zmin}, $\sqrt{N_{max}}$, V_{max}, $\sqrt{dT(B_z, N)}$, and $\sqrt{dT(B_z, V)}$. The fitting scores obtained are an R^2 of 0.58, an RMSE of 21.30 nT, and an MAE of 15.87 nT. The inclusion of *V* in the calculation significantly improves the fit compared with a simpler relationship, as in Khabarova (2008). However, some deviations are noticeable. Super-strong storms, such as the St. Patrick's Day storm of March 17, 2015, and the storm on June 23, 2015, are underestimated by the best model we have in this study. Multi-episodic enhancement of the IMF observed in those cases complicates the identification of the local extrema such that inconsistency arises. Despite its simplicity, the model presented in the present study complements the overall understanding of the complex relationship between solar activity and its effects on Earth's magnetic field. It may help us recognize patterns and relationships between various solar parameters and the resulting geomagnetic disturbances. Beyond that, it is useful for predicting the occurrence and intensity of geomagnetic storms, which is vital for mitigating their potential impacts.

Acknowledgments

We thank the geomagnetic observatories (Kakioka, Japan (Japan Meteorological Agency); Honolulu, Hawaii, and San Juan, Puerto Rico (U.S. Geological Survey); Hermanus, Republic of South African; Alibag, India [India Meteorological Department, National Institute of Information and communications (NICT)-Japan, INTERMAGNET, and many others for their cooperation in making the provisional *Dst* index available.

Supplementary Materials

Table S1. The list of 100 geomagnetic storms used in this study and the associated IMF and solar wind parameters. For most of the cases, our classification is comparable to Chi et al. (2016), Pandya et al. (2019), or Hajra and Sunny (2022).

Day of storm	Time (UT)	Dst_{min} (nT)	B_z (nT)	*N* (cm^{-3})	*V* (km/s)	d$T_{B_z,N}$ (h)	d$T_{B_z,V}$ (h)	d$T_{B_z,Dst}$ (h)	Driver-Storm
28/02/2008	23	−52	−5.1	15.4	498	6	2	5	CIR
09/03/2008	6	−86	−10.6	16.3	487	2	1	1	CIR
27/03/2008	22	−56	−5.4	3.6	642	6	1	3	CIR
04/09/2008	5	−51	−8.7	13.8	488	3	0	2	CIR
11/10/2008	12	−54	−11.0	28.1	352	1	0	3	CIR
22/07/2009	7	−83	−14.5	28.5	341	2	0	2	CIR
15/02/2010	23	−58	−12.0	12.2	325	0	0	4	CME

Continued from Table S1

Day of storm	Time (UT)	Dst_{min} (nT)	B_z (nT)	N (cm^{-3})	V (km/s)	d$T_{B_z,N}$ (h)	d$T_{B_z,V}$ (h)	d$T_{B_z,Dst}$ (h)	Driver-Storm
06/04/2010	15	−81	−6.8	2.5	569	2	2	5	CME
12/04/2010	2	−67	−8.0	11.3	441	0	5	1	CIR
02/05/2010	19	−71	−8.2	37.7	402	3	0	7	CIR
29/05/2010	13	−80	−13.8	9.8	359	8	10	1	CME
04/08/2010	2	−74	−6.1	7.7	597	0	7	2	CME
11/10/2010	20	−75	−11.6	36.4	365	5	2	8	CME
04/02/2011	22	−63	−15.9	27.7	445	2	0	1	CME
01/03/2011	15	−88	−12.1	38.0	382	7	4	2	CME
11/03/2011	6	−83	−10.0	14.5	383	10	0	9	CME
06/04/2011	19	−60	−8.7	12.5	536	3	3	5	CME
28/05/2011	12	−80	−10.7	8.9	508	2	0	2	CME
05/07/2011	1	−59	−8.7	3.6	409	0	0	6	CIR
06/08/2011	4	−115	−19.3	26.8	611	1	1	6	CME
10/09/2011	5	−75	−17.1	37.6	482	3	0	12	CME
17/09/2011	16	−72	−7.2	29.5	537	2	0	5	CME
26/09/2011	24	−118	−24.1	24.4	594	3	0	5	CME
25/10/2011	2	−147	−13.1	25.2	495	4	4	2	CME
01/11/2011	16	−66	−7.9	8.8	432	3	0	3	CME
09/03/2012	9	−145	−16.4	7.1	678	4	4	3	CME
24/04/2012	5	−120	−15.4	23.5	416	2	10	10	CIR
15/07/2012	17	−139	−18.7	20.7	665	5	10	6	CME
01/10/2012	5	−122	−19.2	32.2	394	14	1	3	CME
09/10/2012	9	−109	−14.9	6.7	391	3	0	4	CME
13/10/2012	8	−90	−10.4	6.0	482	1	2	4	CME
14/11/2012	8	−108	−17.4	14.8	397	1	3	4	CME
26/01/2013	24	−52	−8.1	8.0	496	2	1	1	CIR
01/03/2013	11	−55	−13.4	13.0	473	1	0	2	CIR
17/03/2013	21	−132	−14.4	13.4	680	2	1	11	CME
29/03/2013	17	−59	−8.9	10.3	478	3	0	1	CIR
01/06/2013	9	−124	−17.4	39.0	405	3	1	6	CME
29/06/2013	7	−102	−11.9	11.2	404	8	8	7	CME
06/07/2013	19	−87	−11.2	7.6	352	0	1	9	CME
27/08/2013	22	−59	−10.0	23.5	407	2	0	2	CIR
02/10/2013	8	−72	−8.8	22.9	625	0	0	3	CME
30/10/2013	24	−56	−8.1	8.5	373	6	3	2	CIR
08/12/2013	9	−66	−9.8	34.0	488	1	0	5	CIR
19/02/2014	9	−119	−12.9	9.8	474	3	2	3	CME
27/02/2014	24	−97	−12.0	29.7	481	4	2	2	CME
12/04/2014	10	−87	−8.9	7.4	350	1	4	3	CME
30/04/2014	10	−67	−8.1	9.8	308	1	1	0	CME
27/08/2014	10	−79	−13.1	14.8	303	1	2	4	CIR
12/09/2014	24	−88	−11.3	19.3	651	1	4	2	CME
22/12/2014	5	−71	−14.9	24.6	407	2	2	3	CME
23/12/2014	23	−57	−5.0	2.3	527	5	1	8	CME
07/01/2015	12	−107	−17.4	29.4	475	2	2	2	CME
18/02/2015	1	−69	−12.0	10.8	410	6	7	3	CIR
24/02/2015	8	−58	−5.6	12.3	492	2	0	2	CIR

Continued from Table S1

Day of storm	Time (UT)	Dst_{min} (nT)	B_z (nT)	N (cm^{-3})	V (km/s)	d$T_{B_z,N}$ (h)	d$T_{B_z,V}$ (h)	d$T_{B_z,Dst}$ (h)	Driver-Storm
02/03/2015	9	−64	−8.5	11.2	574	4	0	2	CIR
17/03/2015	23	−234	−18.1	33.7	614	9	3	8	CME
11/04/2015	10	−85	−8.5	11.2	574	4	0	2	CME
16/04/2015	24	−88	−6.0	7.0	664	4	1	1	CIR
13/05/2015	7	−82	−8.9	9.9	597	0	0	1	CIR
08/06/2015	9	−67	−14.4	15.1	468	1	0	2	CIR
23/06/2015	5	−198	−22.2	40.4	673	0	0	9	CME
05/07/2015	6	−74	−14.0	37.4	475	4	0	9	CIR
13/07/2015	16	−68	−7.4	7.3	642	1	6	6	CIR
23/07/2015	9	−72	−11.0	8.0	400	3	2	2	CME
16/08/2015	8	−98	−8.4	8.2	514	4	2	1	CME
27/08/2015	21	−103	−10.8	14.0	362	2	5	2	CME
09/09/2015	13	−105	−10.2	14.0	527	4	3	3	CME
07/10/2015	23	−124	−11.2	29.4	462	1	7	8	CIR
07/11/2015	7	−87	−9.9	7.8	677	6	1	2	CME
20/12/2015	23	−166	−17.0	62.7	418	12	7	1	CME
01/01/2016	1	−116	−15.8	25.5	465	9	8	4	CME
20/01/2016	17	−101	−15.8	24.1	461	6	6	4	CIR
03/02/2016	3	−57	−8.3	27.0	358	5	1	1	CIR
18/02/2016	1	−62	−6.6	6.3	552	4	4	7	CIR
06/03/2016	22	−99	−12.7	32.0	552	3	0	2	CIR
08/05/2016	8	−95	−11.5	15.1	485	1	0	6	CIR
03/08/2016	16	−52	−15.1	16.5	430	3	1	1	CIR
23/08/2016	22	−73	−11.1	13.6	433	1	1	2	CIR
02/09/2016	3	−59	−5.9	6.7	570	0	3	5	CIR
29/09/2016	10	−65	−5.2	4.3	692	0	0	3	CIR
13/10/2016	18	−110	−20.8	30.5	437	11	7	1	CME
01/03/2017	22	−61	−4.6	19.0	649	8	0	3	CIR
27/03/2017	15	−70	−8.6	26.6	523	6	0	5	CIR
22/04/2017	17	−51	−4.8	5.8	703	0	10	3	CME
28/05/2017	8	−125	−22.8	62.1	401	5	2	6	CME
16/07/2017	16	−72	−20.2	43.8	506	5	0	3	CME
08/09/2017	2	−122	−24.2	6.4	690	10	0	1	CME
28/09/2017	6	−75	−7.0	7.1	669	6	3	2	CIR
08/11/2017	2	−73	−7.2	32.2	526	5	0	7	CIR
20/04/2018	10	−66	−13.5	49.5	426	4	0	1	CIR
06/05/2018	3	−57	−6.8	36.1	547	3	0	8	CIR
26/08/2018	7	−175	−16.8	20.3	412	3	6	1	CIR
11/09/2018	11	−60	−7.9	7.8	570	1	2	2	CME
07/10/2018	22	−53	−8.3	46.3	503	5	0	6	CIR
05/11/2018	6	−53	−6.5	22.5	571	6	0	1	CIR
14/05/2019	8	−65	−12.7	10.1	537	5	1	2	CME
05/08/2019	21	−53	−7.9	19.9	489	1	0	13	CIR
18/02/2020	17	−52	−8.8	14.2	395	0	0	2	CME
20/04/2020	13	−59	−14.4	34.5	371	2	2	2	CME
25/07/2020	0	−52	−8.0	9.8	375	5	0	3	CIR

References

Abraha, G., Yemane, T., and Kassa, T. (2020). Geomagnetic storms and their impacts on Ethiopian power grid. *Adv. Astron. Space Phys.*, *10*(2), 55–64. https://doi.org/10.17721/2227-1481.10.55-64

Akasofu, S. I. (1981). Energy coupling between the solar wind and the magnetosphere. *Space Sci. Rev.*, *28*(2), 121–190. https://doi.org/10.1007/BF00218810

Al-Feadh, D., and Al-Ramdhan, W. (2019). Large geomagnetic storms drives by solar wind in solar cycle 24. *J. Phys.: Conf. Ser.*, *1234*, 012004. https://doi.org/10.1088/1742-6596/1234/1/012004

Anoke-Uzosike, A., Akala, A. O., and Oyeyemi, E. O. (2024). Sub-daily solar wind-magnetosphere energy transfer during major geomagnetic storms of solar cycle 23. *Adv. Space Res.*, *73*(8), 4314–4328. https://doi.org/10.1016/j.asr.2024.01.007

Bakare, N. O., and Chukwuma, U. V. (2010). Relationship between Dst and solar wind conditions during intense geomagnetic storms. *Indian J. Radio Space Phys.*, *39*(3), 150–155.

Ballatore, P., and Gonzalez, W. D. (2003). On the estimates of the ring current injection and decay. *Earth Planets Space*, *55*(7), 427–435. https://doi.org/10.1186/BF03351776

Blagoveshchensky, D. V., and Sergeeva, M. A. (2019). Impact of geomagnetic storm of September 7-8, 2017 on ionosphere and HF propagation: A multi-instrument study. *Adv. Space Res.*, *63*(1), 239–256. https://doi.org/10.1016/j.asr.2018.07.016

Bolduc, L. (2002). GIC observations and studies in the Hydro-Québec power system. *J. Atmos. Sol. Terr. Phys.*, *64*(16), 1793–1802. https://doi.org/10.1016/S1364-6826(02)00128-1

Borovsky, J. E., and Denton, M. H. (2006). Differences between CME-driven storms and CIR-driven storms. *J. Geophys. Res.: Space Phys.*, *111*(A7), A07S08. https://doi.org/10.1029/2005JA011447

Burton, R. K., McPherron, R. L., and Russell, C. T. (1975). An empirical relationship between interplanetary conditions and *Dst*. *J. Geophys. Res.: Space Phys.*, *80*(31), 4204–4214. https://doi.org/10.1029/JA080i031p04204

Chakraborty, S., and Morley, S. (2020). Probabilistic prediction of geomagnetic storms and the K_p index. *J. Space Wea. Space Climate*, *10*, 36. https://doi.org/10.1051/swsc/2020037

Chappell, C. R., Glocer, A., Giles, B. L., Moore, T. E., Huddleston, M. M., and Gallagher, D. L. (2021). The key role of cold ionospheric ions as a source of hot magnetospheric plasma and as a driver of the dynamics of substorms and storms. *Front. Astron. Space Sci.*, *8*, 746283. https://doi.org/10.3389/fspas.2021.746283

Cheng, L. B., Le, G. M., and Zhao, M. X. (2020). Sun–Earth connection event of super geomagnetic storm on 2001 March 31: The importance of solar wind density. *Res. Astron. Astrophys.*, *20*(3), 36. https://doi.org/10.1088/1674-4527/20/3/36

Chi, Y. T., Shen, C. L., Wang, Y. M., Xu, M. J., Ye, P. Z., and Wang, S. (2016). Statistical study of the interplanetary coronal mass ejections from 1995 to 2015. *Sol. Phys.*, *291*(8), 2419–2439. https://doi.org/10.1007/s11207-016-0971-5

Chi, Y. T., Shen, C. L., Luo, B. X., Wang, Y. M., and Xu, M. J. (2018). Geoeffectiveness of stream interaction regions from 1995 to 2016. *Space Wea.*, *16*(12), 1960–1971. https://doi.org/10.1029/2018SW001894

Crooker, N. U., Feynman, J., and Gosling, J. T. (1977). On the high correlation between long-term averages of solar wind speed and geomagnetic activity. *J. Geophys. Res.: Space Phys.*, *82*(13), 1933–1937. https://doi.org/10.1029/JA082i013p01933

Denton, M. H., Borovsky, J. E., Skoug, R. M., Thomsen, M. F., Lavraud, B., Henderson, M. G., McPherron, R. L., Zhang, J. C., and Liemohn, M. W. (2006). Geomagnetic storms driven by ICME- and CIR-dominated solar wind. *J. Geophys. Res.: Space Phys.*, *111*(A7), A07S07. https://doi.org/10.1029/2005JA011436

Echer, E., Gonzalez, W. D., Tsurutani, B. T., and Gonzalez, A. L. C. (2008). Interplanetary conditions causing intense geomagnetic storms (Dst ≤ -100 nT) during solar cycle 23 (1996–2006). *J. Geophys. Res.: Space Phys.*, *113*(A5), A05221. https://doi.org/10.1029/2007JA012744

Frissell, N. A., Vega, J. S., Markowitz, E., Gerrard, A. J., Engelke, W. D., Erickson, P. J., Miller, E. S., Carl Luetzelschwab, R., and Bortnik, J. (2019). High-frequency communications response to solar activity in september 2017 as observed by amateur radio network. *Space Wea.*, *17*(1), 118–132. https://doi.org/10.1029/2018SW002008

Gonzalez, W. D. (1990). A unified view of solar wind-magnetosphere coupling functions. *Planet. Space Sci.*, *38*(5), 627–632. https://doi.org/10.1016/0032-0633(90)90068-2

Gonzalez, W. D., Tsurutani, B. T., and Clúa de Gonzalez, A. L. (1999). Interplanetary origin of geomagnetic storms. *Space Sci. Rev.*, *88*(3), 529–562. https://doi.org/10.1023/A:1005160129098

Gruet, M. A., Chandorkar, M., Sicard, A., and Camporeale, E. (2018). Multiple-hour-ahead forecast of the dst index using a combination of long short-term memory neural network and Gaussian process. *Space Wea.*, *16*(11), 1882–1896. https://doi.org/10.1029/2018SW001898

Hajra, R., and Sunny, J. V. (2022). Corotating interaction regions during solar cycle 24: A study on characteristics and geoeffectiveness. *Sol. Phys.*, *297*(3), 30. https://doi.org/10.1007/s11207-022-01962-1

Kan, J. R., and Lee, L. C. (1979). Energy coupling function and solar wind-magnetosphere dynamo. *Geophys. Res. Lett.*, *6*(7), 577–580. https://doi.org/10.1029/GL006i007p00577

Kataoka, R., Watari, S., Shimada, N., Shimazu, H., and Marubashi, K. (2005). Downstream structures of interplanetary fast shocks associated with coronal mass ejections. *Geophys. Res. Lett.*, *32*(12), L12103. https://doi.org/10.1029/2005GL022777

Kataoka, R., and Ngwira, C. (2016). Extreme geomagnetically induced currents. *Prog. Earth Planet. Sci.*, *3*(1), 23. https://doi.org/10.1186/s40645-016-0101-x

Khabarova, O. (2008). Current problems of magnetic storm prediction and possible ways of their solving. arXiv: 0805.0547

Kilpua, E., Koskinen, H. E. J., and Pulkkinen, T. I. (2017). Coronal mass ejections and their sheath regions in interplanetary space. *Living Rev. Sol. Phys.*, *14*(1), 5. https://doi.org/10.1007/s41116-017-0009-6

Kim, R. S., Cho, K. S., Moon, Y. J., Dryer, M., Lee, J., Yi, Y., Kim, K. H., Wang, H., Park, Y. D., and Kim, Y. H. (2010). An empirical model for prediction of geomagnetic storms using initially observed CME parameters at the Sun. *J. Geophys. Res.: Space Phys.*, *115*(A12), A12108. https://doi.org/10.1029/2010ja015322

Kim, R. S., Moon, Y. J., Gopalswamy, N., Park, Y. D., and Kim, Y. H. (2014). Two-step forecast of geomagnetic storm using coronal mass ejection and solar wind condition. *Space Wea.*, *12*(4), 246–256. https://doi.org/10.1002/2014SW001033

Kugblenu, S., Taguchi, S., and Okuzawa, T. (1999). Prediction of the geomagnetic storm associated D_{st} index using an artificial neural network algorithm. *Earth Planets Space*, *51*(4), 307–313. https://doi.org/10.1186/BF03352234

Larrodera, C., Nikitina, L., and Cid, C. (2021). Estimation of the solar wind extreme events. *Space Wea.*, *19*(12), e2021SW002902. https://doi.org/10.1029/2021SW002902

Lethy, A., El-Eraki, M. A., Samy, A., and Deebes, H. A. (2018). Prediction of the *Dst* index and analysis of its dependence on solar wind parameters using neural network. *Space Wea.*, *16*(9), 1277–1290. https://doi.org/10.1029/2018SW001863

Lopez, R. E., Wiltberger, M., Hernandez, S., and Lyon, J. G. (2004). Solar wind density control of energy transfer to the magnetosphere. *Geophys. Res. Lett.*, *31*(8), L08804. https://doi.org/10.1029/2003GL018780

Lyatsky, W., and Tan, A. (2003). Latitudinal effect in semiannual variation of geomagnetic activity. *J. Geophys. Res.: Space Phys.*, *108*(A5), 1204. https://doi.org/10.1029/2002JA009467

McNish, A. G. (1940). The magnetic storm of March 24, 1940. *Terr. Magn. Atmos. Electr.*, *45*(3), 359–364. https://doi.org/10.1029/TE045i003p00359

Nagatsuma, T., Kataoka, R., and Kunitake, M. (2015). Estimating the solar wind conditions during an extreme geomagnetic storm: a case study of the event that occurred on March 13–14, 1989. *Earth Planets Space, 67*(1), 78. https://doi.org/10.1186/s40623-015-0249-4

Neugebauer, M., and Goldstein, R. (1997). Particle and field signatures of coronal mass ejections in the solar wind. In N. Crooker, et al. (Eds.), *Coronal*

Mass Ejections (pp. 245). American Geophysical Union. https://doi.org/10.1029/GM099p0245

Nuraeni, F., Ruhimat, M., Aris, M. A., Ratnasari, E. A., and Purnomo, C. (2022). Development of 24 hours Dst index prediction from solar wind data and IMF Bz using NARX. *J. Phys.: Conf. Ser.*, *2214*, 012024. https://doi.org/10.1088/1742-6596/2214/1/012024

Pandey, S. K., and Dubey, S. C. (2017). Impact of solar and interplanetary disturbances on space weather. *Int. Res. J. Adv. Eng. Sci.*, *2*(1), 125–130.

Pandya, M., Bhaskara, V., Ebihara, Y., Kanekal, S. G., and Baker, D. N. (2019). Variation of radiation belt electron flux during CME- and CIR-driven geomagnetic storms: Van Allen probes observations. *J. Geophys. Res.: Space Phys.*, *124*(8), 6524–6540. https://doi.org/10.1029/2019JA026771

Park, W., Lee, J., Kim, K. C., Lee, J., Park, K., Miyashita, Y., Sohn, J., Park, J., Kwak, Y. S. … Yi, Y. (2021). Operational Dst index prediction model based on combination of artificial neural network and empirical model. *J. Space Wea. Space Climate*, *11*, 38. https://doi.org/10.1051/swsc/2021021

Pitňa, A., Šafránková, J., Němeček, Z., Ďurovcová, T., and Kis, A. (2021). Turbulence upstream and downstream of interplanetary shocks. *Front. Phys.*, *8*, 626768. https://doi.org/10.3389/fphy.2020.626768

Podladchikova, T., Petrukovich, A., and Yermolaev, Y. (2018). Geomagnetic storm forecasting service StormFocus: 5 years online. *J. Space Wea. Space Climate*, *8*, A22. https://doi.org/10.1051/swsc/2018017

Pulkkinen, A., Lindahl, S., Viljanen, A., and Pirjola, R. (2005). Geomagnetic storm of 29–31 October 2003: Geomagnetically induced currents and their relation to problems in the Swedish high-voltage power transmission system. *Space Wea.*, *3*(8), S08C03. https://doi.org/10.1029/2004SW000123

Rangarajan, G. K., and Barreto, L. M. (2000). Long term variability in solar wind velocity and IMF intensity and the relationship between solar wind parameters & geomagnetic activity. *Earth Planets Space*, *52*(2), 121–132. https://doi.org/10.1186/BF03351620

Rathore, B. S., Gupta, D. C., and Parashar, K. K. (2014). Relation between solar wind parameter and geomagnetic storm condition during cycle-23. *Int. J. Geosci.*, *5*(13), 1602–1608. https://doi.org/10.4236/ijg.2014.513131

Reiff, P. H., Daou, A. G., Sazykin, S. Y., Nakamura, R., Hairston, M. R., Coffey, V., Chandler, M. O., Anderson, B. J., Russell, C. T., … Genestreti, K. J. (2016). Multispacecraft observations and modeling of the 22/23 June 2015 geomagnetic storm. *Geophys. Res. Lett.*, *43*(14), 7311–7318. https://doi.org/10.1002/2016GL069154

Ren, J., Zong, Q. G., Fu, S. Y., Yang, H. G., Hu, Z. J., Zhang, X. X., Zhou, X. Z., Yue, C., Kistler, L., … Rankin, R. (2023). The dynamics of Earth's cusp in response to the interplanetary shock. *Universe*, *9*(3), 143. https://doi.org/10.3390/universe9030143

Richardson, I. G., Cliver, E. W., and Cane, H. V. (2001). Sources of geomagnetic storms for solar minimum and maximum conditions during 1972–2000. *Geophys. Res. Lett.*, *28*(13), 2569–2572. https://doi.org/10.1029/2001GL013052

Richardson, I. G., and Cane, H. V. (2012). Solar wind drivers of geomagnetic storms during more than four solar cycles. *J. Space Wea. Space Climate*, *2*, A01. https://doi.org/10.1051/swsc/2012001

Saikin, A. A., Zhang, J. C., Smith, C. W., Spence, H. E., Torbert, R. B., and Kletzing, C. A. (2016). The dependence on geomagnetic conditions and solar wind dynamic pressure of the spatial distributions of EMIC waves observed by the Van Allen Probes. *J. Geophys. Res.: Space Phys.*, *121*(5), 4362–4377. https://doi.org/10.1002/2016JA022523

Santoso, A. (2010). Identifikasi kondisi angin surya (*solar wind*) untuk prediksi badai geomagnet. In *Prosiding Pertemuan Ilmiah XXIV HFI Jateng & DIY* (pp. 275–283). Semarang

Shen, X. C., Hudson, M. K., Jaynes, A. N., Shi, Q. Q., Tian, A. M., Claudepierre, S. G., Qin, M. R., Zong, Q. G., and Sun, W. J. (2017). Statistical study of the storm time radiation belt evolution during Van Allen Probes era: CME-versus CIR-driven storms. *J. Geophys. Res.: Space Phys.*, *122*(8), 8327–8339. https://doi.org/10.1002/2017JA024100

Stepanova, M., Antonova, E., Munos-Uribe, F. A., Gordo, S. L. G., and Torres-Sanchez, M. V. (2008). Prediction of geomagnetic storm using neural networks: comparison of the efficiency of the Satellite and ground-based input parameters. *J. Phys.: Conf. Ser.*, *134*, 012041. https://doi.org/10.1088/1742-6596/134/1/012041

Temmer, M. (2021). Space weather: The solar perspective. *Living Rev. Sol. Phys.*, *18*(1), 4. https://doi.org/10.1007/s41116-021-00030-3

Umar, R., Dagang, A. N., Roslan, N. S. I., Syed Zafar, S. N. A., Jusoh, M. H., Yoshikawa, A., Abe, S., and Uozumi, T. (2023). Response of the geomagnetic horizontal component during solar events at RANAU station. *Indian J. Phys.*, *97*(13), 3735–3744. https://doi.org/10.1007/s12648-023-02721-z

Verbanac, G., Vršnak, B., Živković, S., Hojsak, T., Veronig, A. M., and Temmer, M. (2011). Solar wind high-speed streams and related geomagnetic activity in the declining phase of solar cycle 23. *A&A, 533*, A49. https://doi.org/10.1051/0004-6361/201116615

Watari, S. (2018). Intense geomagnetic storms associated with coronal holes under the weak solar-wind conditions of cycle 24. *Sol. Phys.*, *293*(2), 23. https://doi.org/10.1007/s11207-018-1248-y

Webb, D. F., and Howard, T. A. (2012). Coronal mass ejections: observations. *Living Rev. Sol. Phys.*, *9*(1), 3. https://doi.org/10.12942/lrsp-2012-3

Weigel, R. S. (2010). Solar wind density influence on geomagnetic storm intensity. *J. Geophys. Res.: Space Phys.*, *115*(A9), A09201. https://doi.org/10.1029/2009JA015062

Wu, C. C., and Lepping, R. P. (2002). Effect of solar wind velocity on magnetic cloud-associated magnetic storm intensity. *J. Geophys. Res.: Space Phys.*, *107*(A11), 1346. https://doi.org/10.1029/2002JA009396

Wu, C. C., Lepping, R. P., and Gopalswamy, N. (2006). Relationships among magnetic clouds, CMES, and geomagnetic storms. *Sol. Phys.*, *239*(1-2), 449–460. https://doi.org/10.1007/s11207-006-0037-1

Wu, C. C., Liou, K., Lepping, R. P., Hutting, L., Plunkett, S., Howard, R. A., and Socker, D. (2016). The first super geomagnetic storm of solar cycle 24: "The St. Patrick's day event (17 March 2015)". *Earth Planets Space*, *68*(1), 151. https://doi.org/10.1186/s40623-016-0525-y

Xie, X. H., Chen, G. Y., Shang, X. D., and Fang, W. D. (2008). Evolution of the semidiurnal (M_2) internal tide on the continental slope of the northern South China Sea. *Geophys. Res. Lett.*, *35*(13), L13604. https://doi.org/10.1029/2008GL034179

Xu, D., Chen, T., Zhang, X. X., and Liu, Z. (2009). Statistical relationship between solar wind conditions and geomagnetic storms in 1998–2008. *Planet. Space Sci.*, *57*(12), 1500–1513. https://doi.org/10.1016/j.pss.2009.07.015

Xu, S. B., Huang, S. Y., Yuan, Z. G., Deng, X. H., and Jiang, K. (2020). Prediction of the Dst index with bagging ensemble-learning algorithm. *Astrophys. J. Suppl.*, *248*(1), 14. https://doi.org/10.3847/1538-4365/ab880e

Zhou, X. Y., Gedalin, M., Russell, C. T., Angelopoulos, V., and Drozdov, A. Y. (2020). Energetic ion reflections at interplanetary shocks: first observations from ARTEMIS. *J. Geophys. Res.: Space Phys.*, *125*(11), e2020JA028174. https://doi.org/10.1029/2020JA028174